Structure and Dynamics of Homoleptic Beryllocenes: A Solid-State ^{9}Be and ^{13}C NMR Study

Ivan Hung, Charles L. B. Macdonald, and Robert W. Schurko*[a]

Abstract: The correlation between anisotropic ^{9}Be NMR (quadrupolar and chemical shielding) interactions and the structure and dynamics in [Cp_2Be], [Cp^*_2Be], and [$(C_5Me_4H)_2Be$] is examined by solid-state ^{9}Be NMR spectroscopy, as well as by ab initio and hybrid density functional theory calculations. The ^{9}Be quadrupole coupling constants in the three compounds correspond well to the relative degrees of spherical ground-state electronic symmetry of the environment about beryllium. Theoretical computations of NMR interaction tensors are in excellent agreement with experimental values and aid in understanding the origins of NMR interaction tensors and their correlation to molecular symmetry. Variable-temperature (VT) ^{9}Be and ^{13}C NMR experiments reveal a highly fluxional structure in the condensed phase of [Cp_2Be]. In particular, the pathway by which the Cp rings of [Cp_2Be] 'invert' coordination modes is examined in detail using hybrid density functional theory in order to inspect variations of the ^{9}Be NMR interaction tensors. The activation energy for the 'inversion' process is found to be 36.9 kJ mol^{-1} from chemical exchange analysis of ^{13}C VT CP/MAS NMR spectra. The low-temperature (ca. −100 °C) X-ray crystal structures of all three compounds have been collected and refined, and are in agreement with previously reported structures. In addition, the structure of the same Cp_2Be crystal was determined at 20 °C and displays features consistent with increased intramolecular motion, supporting observations by ^{9}Be VT NMR spectroscopy.

Keywords: ab initio calculations · beryllium · metallocenes · NMR spectroscopy · X-ray diffraction

Introduction

Owing to its unusual structure, much work has been devoted to the study of bis(cyclopentadienyl)beryllium, [Cp_2Be] ($Cp = C_5H_5$), since its preparation in 1959.[1] It was clear from the outset that [Cp_2Be] did not possess a highly symmetric geometry (as ferrocene does) because of various measured properties,[2,3] including the dipole moment observed in solution.[1] A structure for the compound was first postulated by Almenningen and co-workers based upon data from vapour-phase electron diffraction.[4] The hypothesized structure consisted of two parallel, staggered Cp rings and a beryllium atom lying at one of two alternate positions along the fivefold principal axis of the molecule, 1.485(5) Å from one ring and 1.98(1) Å from the other (Scheme 1, **I**). The report of such an unusual C_{5v} structure quickly drew the attention of many researchers. Further investigation provided support for the existence of structure **I**.[4–7] Furthermore, a LCAO MO study comparing **I** and **II** for [Cp_2Be] found the C_{5v} geometry to have a lower total electronic energy,[8] and analysis of Raman and IR spectral data estimated the average time spent by the Be at each of the alternate positions to be on the order of 10^{-13} to 10^{-12} s.[9]

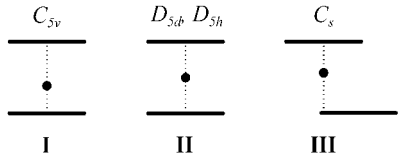

Scheme 1. Proposed structures of [Cp_2Be] with (**I**) C_{5v}, (**II**) D_{5h}/D_{5d} and (**III**) C_s symmetry.

In 1972, Wong and co-workers reported the first low-temperature (−120 °C) X-ray crystal structure analysis of [Cp_2Be].[10] The two Cp rings were found to be more or less parallel (as in ferrocene) and staggered with respect to each other, however, one of the rings appeared as if it had "slipped" sideways with its centroid 1.20 Å away from the ideal D_{5d} fivefold axis, resulting in a structure in which the Be atom is roughly equidistant from all five carbons of one Cp ring and bound to only one carbon on the other Cp ring (dubbed the "slip" sandwich structure; **III** in Scheme 1).

[a] I. Hung, Prof. C. L. B. Macdonald, Prof. R. W. Schurko
Department of Chemistry and Biochemistry
University of Windsor, 393-A Essex Hall
Windsor, ON, N9B 3P4 (Canada)
Fax: (+1) 519-973-7098
E-mail: rschurko@uwindsor.ca

Supporting information for this article is available on the WWW under http://www.chemeurj.org/ or from the author.

 DOI: 10.1002/chem.200400404

The discovery of a new [Cp_2Be] structure quickly led researchers to re-evaluate previous data. In one such study it was noted that the bonding in the 'slip' sandwich should be described more appropriately as having polyhapto π coordination (η^x) rather than a σ bond between Be and the singly bound Cp ring, due to the parallel arrangement of the Cp rings.[11] Wong and co-workers went on to re-examine the crystal structure of Cp_2Be at room temperature,[12,13] and found a similar structure to the one reported at −120 °C, but with notable differences. These observations, along with the appearance of a single resonance in solution ^1H and ^9Be NMR spectra,[14,15] led to the proposition that [Cp_2Be] had a highly fluxional structure which underwent rapid ring reorientation about their centroids *and* possibly exchange of the Be atom between the two half-occupied crystallographic positions. A number of theoretical studies were performed to examine the bonding in [Cp_2Be] and determine its lowest energy structure.[16–26] In contrast to previous results, all calculations favoured structures **II** and **III** energetically over the C_{5v}-type structures. Further investigation of [Cp_2Be] by various techniques contributed increasing support for structure **III**.[27–32] In fact, comparison of IR spectra of vapor, solution and solid [Cp_2Be] suggests that some form of **III** actually persists in all phases.[33]

More recently, studies using Car–Parrinello molecular dynamics (MD) calculations,[34] and the synthesis of various other beryllocenes with substituted Cp rings has been reported. MD calculations predict that the ground state for [Cp_2Be] should have a structure resembling that of **III**, and that this structure is energetically favoured over both the D_{5d} and D_{5h} geometries by approximately 10 kJ mol^{-1}.[35] Furthermore, two dynamic processes are observed in accordance with the initial proposition by Wong and co-workers:[13] 1) 1,2-sigmatropic rearrangement of the η^1-ring wherein the Be−(η^1-Cp) bond moves from one carbon atom to an adjacent carbon atom, and 2) intramolecular exchange caused by 'inversion' of the coordination modes between the η^5- and η^1-Cp rings.[36] These two processes are calculated to have activation barriers of 5 and 8 kJ mol^{-1} at 400 K, and rates of 1–4 and 0.3–1.5 ps^{-1}, respectively, in close agreement with the barrier (5.2 kJ mol^{-1}) for Cp ring inversion determined from variable-temperature ^{13}C solution NMR spectra of [Cp_2Be].[31] A number of substituted- and mixed-Cp′ beryllocenes have been prepared by Conejo and co-workers, including [Cp^*_2Be] ($Cp^* = C_5Me_5$), [$(C_5Me_4H)_2Be$] and [$Cp^*Be(C_5Me_4H)$].[37–39] Through the reaction of [Cp^*_2Be] and [$(C_5Me_4H)_2Be$] with 2,6-dimethylphenyl isocyanide (CNXyl), Conejo and co-workers have provided experimental chemical evidence for the presence of the η^5,η^1-isomer of [Cp^*_2Be] in solution and sigmatropic rearrangement of the η^1-ring in [$(C_5Me_4H)_2Be$].[40] This conclusion rests on the reasonable assumption that the observed iminoacyl products result from coupling of the η^5,η^1 isomers of the corresponding beryllocenes with CNXyl. Similarly, evidence for molecular rearrangement ('inversion') of the η^5- and η^1-rings has also been provided by reactions of [$Cp^*Be(C_5Me_4H)$] with CNXyl.[41]

Solid-state NMR spectroscopy of metal nuclei at the heart of metallocenes is a powerful means for studying structure and dynamics in these molecules, since the orientation-dependent NMR tensors are very sensitive to changes in the electronic environment about the nuclei. Relevant solid-state NMR examples include[42] ^{25}Mg NMR spectroscopy of [Cp_2Mg],[43] ^{27}Al NMR spectroscopy of [$Cp^*_2Al]^+$,[44] ^{11}B NMR spectroscopy of [$Cp^*_2B]^+$ and [Cp^*_2BMe],[45] ^7Li NMR spectroscopy of lithocenes,[46] ^{23}Na NMR spectroscopy of CpNa-TMEDA,[47] ^{119}Sn and ^{207}Pb NMR spectroscopic characterization of a variety of stannocenes and plumbocenes,[48,49] single-crystal ^{59}Co NMR spectroscopy of [$Cp_2Co]NO_3{\cdot}H_2O$,[50] and a ^{171}Yb CP/MAS NMR study of [Cp'_2Yb^{II}] complexes.[51]

Although ^9Be is a half-integer quadrupolar nucleus with a small nuclear quadrupole moment (nuclear spin $I = 3/2$, $Q = 5.288 \times 10^{-30}$ m^2),[52,53] 100 % natural abundance and receptivity of 78.7 compared to ^{13}C, there are relatively few examples of solid-state ^9Be NMR spectroscopic studies in the literature, likely because of the extreme toxicity of beryllium-containing compounds. Solid-state ^9Be NMR spectra of [$Be(acac)_2$] have been reported,[42] along with studies that focus mainly upon the characterization of beryllium sites in minerals.[42,54–63] The ^9Be quadrupole coupling constants measured for these compounds all fall within the relatively narrow range of 30–700 kHz. To the best of our knowledge, there are no reported solid-state ^9Be NMR studies on organometallic beryllium complexes, although various organometallic complexes have been studied by solution ^9Be NMR spectroscopy and ab initio calculations.[14,31,42,64–66]

Herein we present the solid-state ^9Be and ^{13}C NMR study of [Cp_2Be] (**1**), [Cp^*_2Be] (**2**), and [$(C_5Me_4H)_2Be$] (**3**) (see Figure 1). Experimentally determined and theoretically calculated ^9Be electric field gradient (EFG) and chemical shielding (CS) tensors are reported, and the relationship between these NMR interaction tensors and the molecular structure of the beryllocenes is probed. There has been much recent progress in understanding the fluxional structures of beryllocenes, yet not much work on the study of the intramolecular dynamics present in the solid state has been reported. To address this, variable-temperature (VT) ^9Be and ^{13}C NMR, as well as $^{13}C/^9Be/^1H$ triple-resonance experiments, are utilized to probe the changes in the NMR interaction tensors and isotropic NMR signals with intramolecular dynamics which occur on the dynamic NMR timescale.

Results and Discussion

X-ray crystallography: Representative crystals from the samples subsequently used for the NMR experiments were subjected to X-ray crystallographic analysis to confirm the structural features of the materials. Figure 1a shows one molecule from each of the low-temperature (either −100 °C or −120 °C) crystal structures of **1**–**3**; the metrical parameters and the geometries of the refined structures agree with those reported previously (Table 1). Crystallographic data for the same crystal of **1** was also collected at 20 °C and refined. As illustrated in Figure 1b, the model for the higher temperature structure exhibits significantly larger thermal ellipsoids than that of the lower temperature structure. In

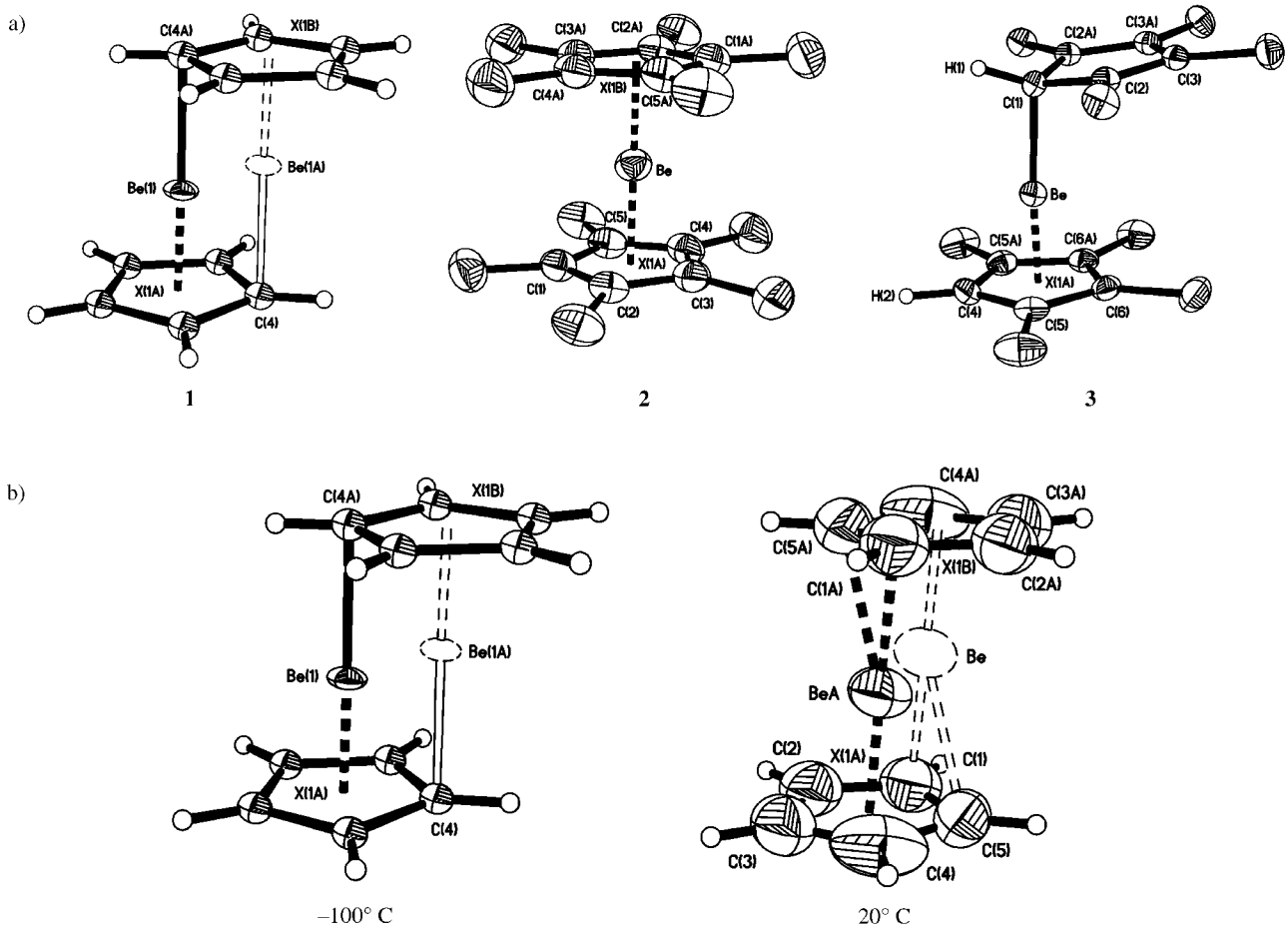

Figure 1. a) Molecules of **1**–**3** from their respective crystal structures; b) molecular structures of **1** at −100 °C and 20 °C.

addition, whereas the structure at −100 °C is best described as having an η^5,η^1 arrangement, the model at 20 °C is better described as exhibiting an η^5,η^2 coordination of the Cp rings. Furthermore, the inversion-related positions of the Be atoms are significantly closer together at 20 °C (0.828 Å) than at low temperature (1.230 Å) and there is less "slippage" of the two Cp rings at higher temperature. These related structural features are consequences of the increased inter-ring separation at higher temperature (3.406 Å at 20 °C versus 3.346 Å at −100 °C) that is accommodated by the increase of the crystallographic *c* axis (from 10.550(2) Å to 10.827(2) Å using the $P2_1/c$ space group for each unit cell). While the structural features observed by the X-ray diffraction snapshots are consistent with significantly greater disorder in the structure of [Cp_2Be] at 20 °C than at −100 °C, the NMR experiments described herein provide more detailed information about the nature of the motion in the solid state.

Solid-state ^{9}Be NMR spectroscopy: Experimental ^{9}Be MAS NMR spectra of **1**–**3** are shown in Figure 2 along with corresponding numerical (Figures 2a, b) and analytical (Figure 2c) simulations. The ^{9}Be quadrupolar coupling constants of **1** and **2** are relatively small in magnitude (0.41(2) and 0.23(2) MHz, respectively), resulting in the absence of observable second-order quadrupolar effects in the central transition powder pattern. Thus, acquisition of satellite transition (SATRAS) NMR spectra is necessary to extract the ^{9}Be quadrupolar parameters (EFG and CS parameters derived from spectral simulations are shown in Table 2 for **1**–**3**). In contrast to **1** and **2**, the spectrum of **3** displays a characteristic second-order quadrupolar powder pattern which yields $C_Q = 0.61(5)$ MHz and $\eta_Q = 0.13(7)$. Notably, as the spherical symmetry decreases in the order **2**→**1**→**3**, the magnitude of $C_Q(^9\text{Be})$ increases correspondingly: 0.23→0.41→0.61 MHz. It is intriguing that the $C_Q(^9\text{Be})$ of **1** has an intermediate value compared to **2** and **3**, which reflects its unusual equilibrium geometry consisting of η^5,η^x coordination to the Cp rings.

The experimental static ^{9}Be NMR spectra of **1**–**3** are shown in Figure 3 along with simulations including and excluding the effects of CSA. Comparison of simulated spectra that only take into account the ^{9}Be nuclear quadrupolar interaction (top traces) with the experimental spectra (bottom traces) immediately indicates the presence of Be CSA (confirmed by the simulations shown in the middle traces). Although ^{9}Be EFG parameters for the three species are markedly different, the CS parameters (i.e., δ_{iso}, Ω, and κ in Table 2) appear to be relatively similar. The differences appear small because of the relatively small CS range of beryllium (ca. +25 to −25 ppm).[67,68] In light of this, we note that the CSA of **1** is significantly greater than the other two

Table 1. Summary of X-ray crystallographic data for **1–3**.

Compound	**1**	**1**	**2**	**3**
empirical formula	$C_{10}H_{10}Be$	$C_{10}H_{10}Be$	$C_{20}H_{30}Be$	$C_{18}H_{26}Be$
formula weight [g mol^{-1}]	139.19	139.19	279.45	251.40
temperature [°C]	20	−100	−120	−100
wavelength [Å]	0.71069	0.71069	0.71069	0.71069
crystal system	monoclinic	monoclinic	monoclinic	orthorhombic
space group	$P2_1/n$[a]	$P2_1/c$	$C2/c$	$Pnma$
a [Å]	5.8901(6)	5.9255(6)	15.1014(13)	12.9448(10)
b [Å]	7.6768(9)	7.4919(10)	12.2367(10)	15.7223(13)
c [Å]	9.3233(14)	10.5501(14)	9.5512(8)	7.6583(6)
α [°]	90	90	90	90
β [°]	92.297(11)	121.345(8)	95.020(2)	90
γ [°]	90	90	90	90
volume [Å^3]	421.23(9)	400.00(9)	1758.2(3)	1558.6(2)
Z	2	2	4	4
ρ_{calcd} [g cm^{-3}]	1.097	1.156	1.056	1.071
ν [mm^{-1}]	0.059	0.063	0.057	0.058
$F(000)$	148	148	616	552
crystal size [mm]	0.50×0.30×0.30	0.50×0.30×0.30	0.70×0.50×0.30	0.60×0.50×0.30
q range [°]	3.44–27.56 3.54–27.49	2.15–27.55	2.59–24.98	
index ranges:	$-7 \le h \le 7$	$-7 \le h \le 7$	$-19 \le h \le 19$	$-15 \le h \le 15$
	$-9 \le k \le 9$	$-9 \le k \le 9$	$-15 \le k \le 15$	$-18 \le k \le 18$
	$-11 \le l \le 12$	$-13 \le l \le 13$	$-12 \le l \le 12$	$-9 \le l \le 9$
reflections collected	3964	3273	8454	9848
independent reflections	976	904	2035	1406
R(int)	0.0351	0.0354	0.0274	0.0525
completeness to q [%]	99.9	98.2	100.0	98.8
absorption correction	none	none	none	none
refinement method	full-matrix least-squares on F^2			
data/restraints/parameters	976/0/56	904/0/57	2035/0/97	1406/0/105
goodness of fit on F^2	1.007	1.447	1.019	1.244
final R indices [$I > 2\sigma(I)$]				
$R1$	0.0803,	0.1052,	0.0582,	0.0872,
$wR2$	0.2583	0.2219	0.1559	0.1928
R indices (all data)				
$R1$	0.1477,	0.1105,	0.0863,	0.0983
$wR2$	0.3188	0.2240	0.1759	0.1980
largest diff. peak	0.237 and	0.248 and	0.183 and	0.310 and
and hole [e A^{-3}]	−0.113	−0.277	−0.151	−0.216
extinction coefficient	0.13(6)	0.07(2)		

[a] The $P2_1/n$ unit cell of [Cp_2Be] at 20°C corresponds to a $P2_1/c$ cell with unit cell parameters: $a = 5.8901(6)$, $b = 7.6768(9)$, $c = 10.8266(12)$ Å, $\beta = 120.63(1)$°.

compounds, and also that all three species display chemical shielding spans on the order of the entire known Be chemical shift range for diamagnetic complexes. The large metal CSA caused by coordination to Cp′ ligands are consistent with observations from $[Cp_2^*Al]^+$,[44] $[Cp_2^*B]^+$ and $[Cp_2^*BMe]$.[45] It is also interesting to note that the Be nuclei become more shielded with increasing hapticity (i.e., δ_{iso}(**3**):$\eta^5,\eta^1 > \delta_{iso}$(**1**):$\eta^5,\eta^x > \delta_{iso}$(**2**):$\eta^5,\eta^5$), which also corresponds to the trend observed for $[Cp_2^*Al]^+$, $[Cp_2^*B]^+$ and $[Cp_2^*BMe]$.

Aside from the expected anisotropic powder pattern, the static ^{9}Be NMR spectrum of **1** reveals a small additional peak at the isotropic position of the powder pattern (marked with an asterisk in Figure 3a). Variable-temperature static ^{9}Be NMR experiments were performed on **1** to explore the possibility of observing the effects of intramolecular dynamics on the powder pattern (Figure 4). As the temperature is raised, the isotropic peak gradually increases in magnitude until about 60°C, where the anisotropic powder pattern completely collapses leaving only the very sharp isotropic signal; this process is reversible and no dynamic "coalescence point" is observed. The lack of a coalescence temperature suggests the onset of a phase change in which the [Cp_2Be] molecules start to undergo motion(s) capable of completely averaging both the CS and EFG tensors. The large ^{9}Be CSA patterns for all of the beryllocenes suggest that this peak does not result from an intermediate structure of higher symmetry, but rather from a portion of the molecules in the condensed phase undergoing isotropic "solution-like" motion (even at ambient temperature). The sharp isotropic peak and complete absence of CSA effects in the spectrum acquired at 60°C result from melting of the sample (m.p. 59°C).[69] This process is reversible, since identical static spectra are obtained after cooling the sample from 60°C, meaning that it is possible to recrystallize [Cp_2Be] from the melt.

VT ^{9}Be NMR experiments were also performed for **2** and **3**. The VT ^{9}Be SATRAS NMR spectra of **2** show a change

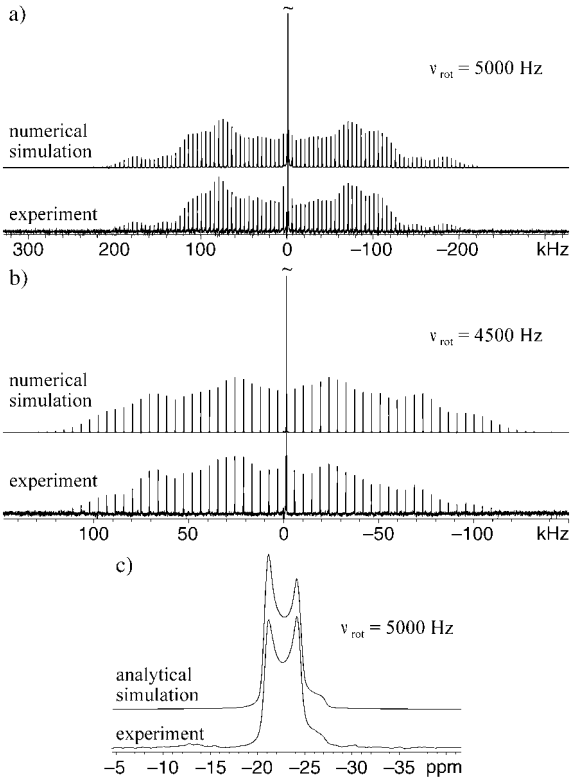

Figure 2. ^{9}Be MAS NMR spectra of a) **1**, b) **2**, and c) **3** at $B_0 = 9.4$ T. Simulations of **1** and **2** were performed with SIMPSON and that of **3** with WSOLIDS.

Table 2. Experimental ^{9}Be and ^{13}C NMR parameters.

Parameter	**1**		**2**		**3**[a]
nucleus	^{9}Be	^{13}C	^{9}Be	^{13}C[b]	^{9}Be
$\lvert C_Q \rvert$ [MHz]	0.41(2)	–	0.23(2)	–	0.61(5)
η_Q[c]	0.25(5)	–	0.55(5)	–	0.13(7)
δ_{iso} [ppm][d]	−21(1)	108.2(2)	−24.4(7)	110(3)	−19.8(5)
Ω [ppm][e]	65(2)	130(2)	55(5)	112(1)	54(4)
κ[f]	0.83(4)	1.0	0.86(7)	1.0	0.85(8)
δ_{11} [ppm][g]	2.5	151.5	−4.8	147.3	−0.5
δ_{22} [ppm]	−3	151.5	−8.6	147.3	−4.5
δ_{33} [ppm]	−62.5	21.5	−59.8	35.3	−54.5
α[h] [°]	0	–	90	–	90
β [°]	38(5)	–	28	–	4(2)
γ [°]	0	–	44	–	0

[a] Carbon CS parameters for $(C_5Me_4H)_2Be$ are shown in Table 3. [b] Carbon chemical shift tensor corresponds to aromatic carbons. [c] Quadrupolar asymmetry parameter, $\eta_Q = (V_{11} - V_{22})/V_{33}$. [d] Isotropic shift, $\delta_{iso} = (\delta_{11} + \delta_{22} + \delta_{33})/3$. [e] Span of the CS tensor, $\Omega = \delta_{11} - \delta_{33}$. [f] Asymmetry of the CS tensor, $\kappa = 3(\delta_{22} - \delta_{iso})/\Omega$. [g] Principal components of the CS tensor from least to most shielded: $\delta_{11} \geq \delta_{22} \geq \delta_{33}$. [h] Euler angles α, β, γ for rotation of the EFG principal axis system into the CS principal axis system.

in isotropic shift from $\delta = -23.1$ to -25.7 ppm, as well as an apparent increase in C_Q(^{9}Be), as the temperature is decreased from 110 °C to −100 °C (Figure 1 in the Supporting Information). The origin of the temperature-dependent chemical shift variation is unknown; however, the lower values of C_Q with increased temperature is well understood, and normally attributed to motional averaging of the EFG tensors due to increased intramolecular motions at higher temperatures.[70,71] VT ^{9}Be NMR experiments on **3** do not show any observable changes with temperature.

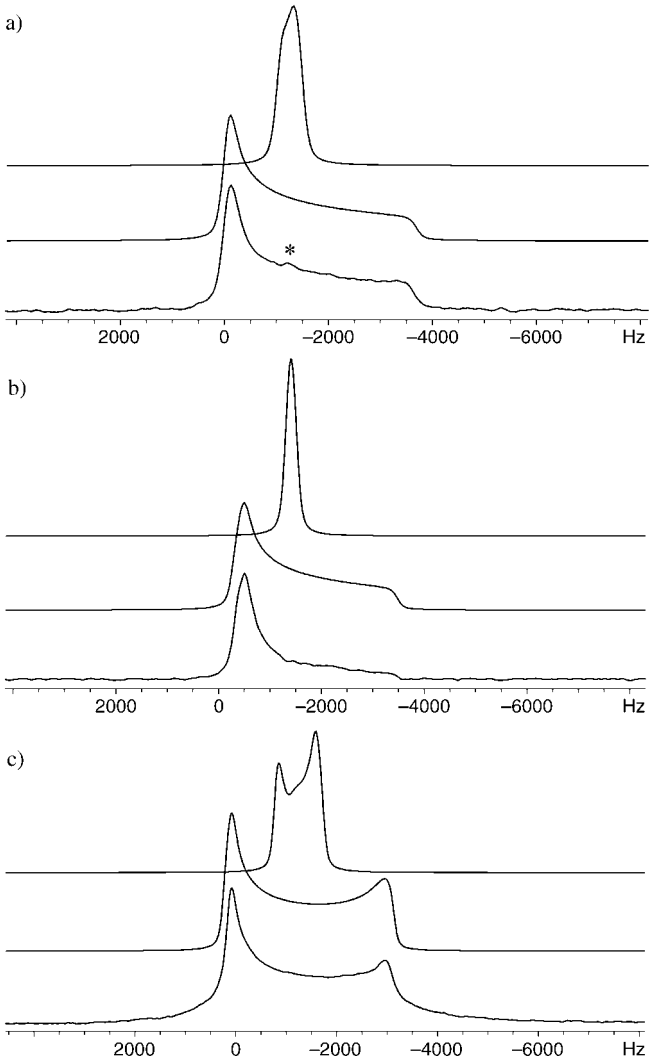

Figure 3. Static ^{9}Be NMR spectra of a) **1**, b) **2**, and c) **3** at $B_0 = 9.4$ T. Traces: bottom: experimental; middle: simulation including CSA; top: simulation excluding CSA. Asterisk (*) points out resonance at the isotropic position.

Solid-state ^{13}C NMR spectroscopy: The ^{13}C CP/MAS NMR spectra of **1** and **2** (Figure 5a, 5b) display spinning-sideband manifolds indicative of carbon CSA in the aromatic region, which is common for metallocenes. The aromatic carbon sites have the following CSA parameters: **1**: $\delta_{iso} = 108.2(2)$ ppm, $\Omega = 130(2)$ ppm, $\kappa = 1.0$; **2**: $\delta_{iso} = 110(3)$ ppm, $\Omega = 112(1)$ ppm, $\kappa = 1.0$, while the Me carbon nuclei in **2** have $\delta_{iso} = 10.7(5)$ ppm—comparable to data reported for other metallocenes. Both the axial symmetry of the aromatic carbon CS tensors (i.e., $\kappa = 1.0$) and the observation of a single Cp′ resonance are attributed to the fast reorientation of the Cp′ moieties about their ring centroids.[43,44,72,73] Due to the lower overall molecular symmetry of **3**, its ^{13}C NMR spectra (Figure 5c) are relatively complex compared to those of **1** and **2**. By spinning the sample at a frequency of $\nu_{rot} = 15$ kHz, the spinning sidebands are removed, leaving

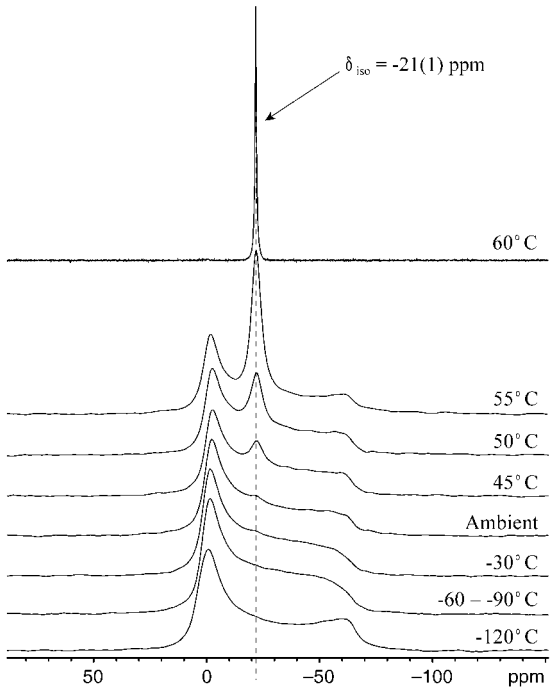

Figure 4. Static ^{9}Be VT NMR spectra of **1** at $B_0 = 9.4$ T.

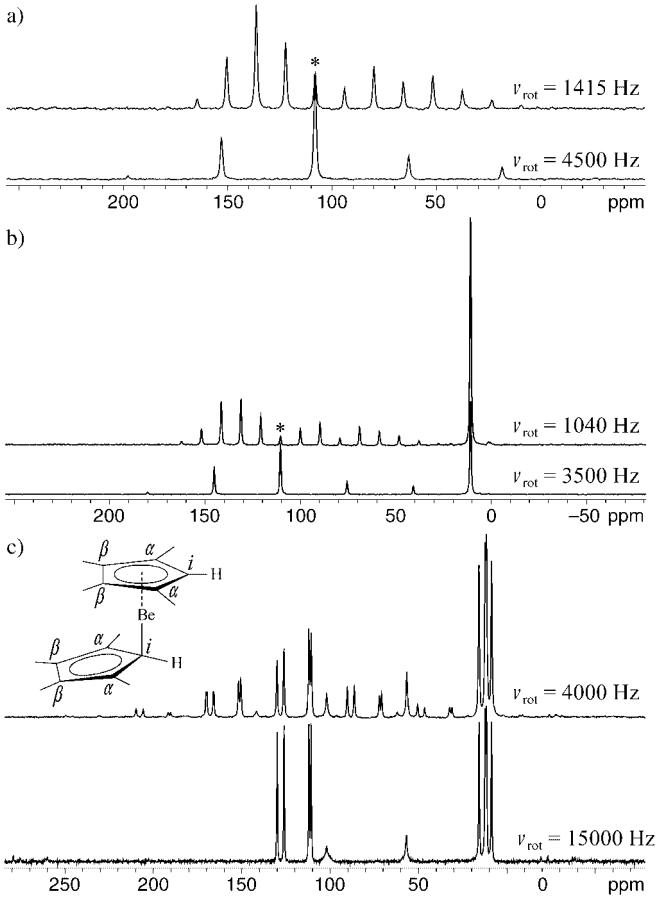

Figure 5. ^{13}C CP/MAS NMR spectra of a) **1**, b) **2**, and c) **3** at different spinning frequencies. Inset in (c) shows the labeling scheme of the carbon sites in **3**.

only the isotropic peaks for each of the distinct carbon environments. Analysis of the sideband manifolds in the slow-spinning ($\nu_{rot} = 4.0$ kHz) spectrum by the method of Herzfeld and Berger yields the carbon CS parameters shown in Table 3. From high to low frequency, the ^{13}C signals are assigned to the η^1: α- (130.1 ppm), η^1: β- (126.0 ppm), η^5: β- (112.0 ppm), η^5: α- (110.6 ppm), η^5: *i*- (101.9 ppm) and η^1: *i*- $(C_5Me_4H)_2Be$ carbons (56.8 ppm); the four remaining peaks are collectively assigned to the eight methyl groups. These assignments were based primarily on the values of the CS parameters (i.e., δ_{iso}, Ω and κ) of each carbon site. As mentioned above, the axial symmetry ($\kappa = 1$) of Cp′ carbon CS tensors has been shown to arise from time-averaging of the δ_{11} and δ_{22} components caused by reorientation of the carbocycles,[43,44,72,73] also in agreement with the observation of a single ^{13}C NMR resonance for both rings in solution.[37] The signals at $\delta = 112.0$ and 110.6 ppm are therefore assigned to the η^5-Cp′ carbon atoms and those at $\delta = 130.1$ and 126.0 ppm can be attributed to the η^1-Cp′ carbon atoms. Differentiation of the α and β sites in each of the C_5Me_4H rings was accomplished by comparison of experimental values of Ω and κ with theoretical values obtained from ab initio calculations (Table 3). Based upon ^{13}C/^{9}Be/^{1}H CP/TRAPDOR[74] experiments (vide infra) and their chemical shifts ($\delta_{iso} = -100$–130 ppm is characteristic of η^5-Cp′ carbon atoms), the signals at $\delta = 101.9$ and 56.8 ppm are assigned to the η^5: *i*-Cp′ and η^1: *i*-Cp′ sites, respectively.

The ^{13}C VT CP/MAS spectra of **1** are shown in Figure 6. The resonance at $\delta_{iso} = 108.2$ ppm gradually splits into two peaks upon cooling to −2 °C ($\delta_{iso} = 110.0$ and 106.3 ppm) and remains as such all the way down to −110 °C. The average δ_{iso} of the two peaks found at low temperature is equal to the isotropic shift of the carbon signal at ambient temperature, being highly indicative of chemical exchange. A detailed analysis of the spectra between the temperatures +3 to −5 °C (see Figure 2 in the Supporting Information for details) reveals the coalescence point (≈ −1 °C) and activation energy ($E_a = 36.9$ kJ mol^{-1}) for the chemical exchange process. The measured E_a for the 'inversion' process lies intermediate to values calculated with the PRDDO method (62.8–129.7 kJ mol^{-1}),[17] and those obtained from MD calculations at 400 K (8 kJ mol^{-1})[36] and ^{9}Be-^{13}C spin–spin coupling in solution ^{13}C VT NMR spectra (5.2 kJ mol^{-1}).[31] It is worth mentioning that although the ^{13}C CP/MAS spectra of **1** at higher temperatures (ca. 40–60 °C) resemble the spectrum obtained at ambient temperature, the optimal contact time was shorter (5 ms) and required the acquisition of many more transients to achieve reasonable intensity than spectra at lower temperatures. The apparent loss in cross-polarization efficiency at higher temperatures may be caused by increased rates of motion which serve to partially average ^{1}H–^{13}C dipolar coupling. The effects of chemical exchange in the ^{13}C NMR spectra of **1** correlate well with observations from ^{9}Be VT NMR spectra: as the temperature is lowered, the time spent by the Be atom at each crystallographic site increases compared to the time scale of the NMR experiment, resulting in the observation of a single Be site. At the same time, the equivalence of the Cp carbons caused by rapid motion of the Be is nullified and results in

Table 3. Experimental and theoretical ^{13}C NMR CS parameters of **3**.[a]

Site	δ_{11} [ppm][b]	δ_{22} [ppm]	δ_{33} [ppm]	δ_{iso} [ppm]	Ω [ppm]	κ [ppm]
			experimental			
η^5:α-C_5Me_4H[c]	151.6	151.6	28.7	110.6	122.9	1.00
η^5:β-C_5Me_4H	151.5	151.5	32.9	112.0	118.6	1.00
η^5:*i*-C_5Me_4H	153.1	115.4	37.2	101.9	115.9	0.35
η^1:α-C_5Me_4H	212.0	145.6	32.7	130.1	179.3	0.26
η^1:β-C_5Me_4H	204.8	129.8	43.5	126.0	161.3	0.07
η^1:*i*-C_5Me_4H	–	–	–	56.8	–	–
			RHF/6–31G**			
η^5:α	165.0	125.8	15.2	102.0	149.8	0.48
η^5:β	165.1	130.9	20.1	105.4	145.0	0.53
η^5:*i*	153.4	91.7	15.3	86.8	138.1	0.11
η^1:α	225.6	135.9	16.0	125.8	209.7	0.14
η^1:β	206.3	116.9	29.6	117.6	176.7	−0.01
η^1:*i*	73.0	19.3	9.4	33.9	63.6	−0.69
			RHF/6–311G**			
η^5:α	159.8	117.6	0.5	92.6	159.3	0.47
η^5:β	158.9	122.7	5.4	95.6	153.5	0.53
η^5:*i*	146.5	80.3	2.7	76.5	143.8	0.08
η^1:α	226.5	127.9	1.8	118.8	224.7	0.12
η^1:β	206.1	106.3	15.2	109.2	190.9	−0.05
η^1:*i*	61.9	6.9	−3.8	21.7	65.7	−0.67
			RHF/6–311+G**			
η^5:α	161.1	119.0	1.7	93.9	159.4	0.47
η^5:β	160.4	124.3	6.7	97.1	153.7	0.53
η^5:*i*	147.5	81.6	3.8	77.6	143.6	0.08
η^1: α	227.6	129.5	3.2	120.1	224.4	0.13
η^1:β	207.5	108.3	16.5	110.8	191.0	−0.04
η^1:*i*	63.4	8.4	−2.4	23.2	65.8	−0.67
			B3LYP/6–31G**			
η^5:α	167.1	135.0	34.4	112.1	132.7	0.52
η^5:β	167.9	140.6	40.2	116.2	127.7	0.57
η^5:*i*	157.7	98.8	29.9	95.5	127.8	0.08
η^1:α	210.9	143.8	34.6	129.8	176.2	0.24
η^1:β	201.0	133.8	48.0	127.6	153.0	0.12
η^1:*i*	91.7	32.9	26.6	50.4	65.0	−0.81
			B3LYP/6–311G**			
η^5:α	172.0	134.2	24.3	110.2	147.7	0.49
η^5:β	171.3	140.1	30.7	114.0	140.6	0.56
η^5:*i*	160.2	94.5	23.6	92.8	136.6	0.04
η^1:α	222.3	143.2	25.8	130.5	196.5	0.20
η^1:β	210.9	131.4	39.4	127.2	171.6	0.07
η^1:*i*	89.6	27.3	19.1	45.3	70.4	−0.77
			B3LYP/6–311+G**			
η^5:α	172.9	135.4	25.1	111.1	147.8	0.49
η^5:β	172.7	142.1	30.8	115.2	141.9	0.57
η^5:*i*	160.3	96.2	24.2	93.5	136.1	0.06
η^1:α	223.2	143.7	25.7	130.9	197.6	0.20
η^1:β	212.8	132.6	40.7	128.7	172.2	0.07
η^1:*i*	92.7	25.9	18.6	45.7	74.1	−0.80

[a] All CS parameters are defined as in Table 2. [b] Carbon shielding values were converted to shifts by referencing to the carbon shielding of CO as $\delta_{iso}=187.1$ ppm (see Experimental Section). [c] Labeling Scheme of carbon sites can be found in inset of Figure 5c.

observation of the two nonequivalent Cp rings. However, the low temperatures employed are insufficient to slow down the very rapid reorientation of the Cp rings about their five-fold axes, and therefore, the carbon sites within each of the Cp rings cannot be differentiated.

$^{13}C/^{9}Be/^{1}H$ VT CP/TRAPDOR NMR experiments were performed in order to examine the intramolecular dynamics present in all three compounds. By examining the loss in intensity observed in TRAPDOR spectra, it is possible to determine the presence and relative magnitudes of dipolar couplings between beryllium and various carbon nuclei. The $^{13}C/^{9}Be/^{1}H$ CP/TRAPDOR spectrum of **1** (not shown) yields an integrated intensity, including the spinning sidebands, of 0.7 compared to the CP/MAS experiment (normalized integrated intensity of 1.0). Only slight increases in the TRAPDOR effect were observed upon lowering the temperature, and are not very diagnostic in terms of examining temperature-dependent dynamics.

The $^{13}C/^{9}Be/^{1}H$ CP/TRAPDOR spectrum of **3** is shown in Figure 7. As expected, the TRAPDOR effect is most pronounced for the η^1: *i*-Cp′ carbon (marked with *), which is directly bound to the beryllium. Interestingly, the methyl resonances show a larger decrease in intensity under TRAPDOR conditions than the aromatic Cp′ carbons; the origin of this effect is unknown at this time. VT experiments (not shown) from 80 °C to −100 °C do not display any differences in the TRAPDOR effect compared to spectra acquired at ambient temperature. This suggests that the carbocycles in **3** display relatively little motion and are rather rigid in contrast to **1** and **2**.

$^{13}C/^{9}Be/^{1}H$ VT CP/TRAPDOR experiments for **2** are shown in Figure 8. At ambient temperature and higher, TRAPDOR and control spectra are almost identical, perhaps indicating little or motionally averaged ^{13}C–^{9}Be dipolar coupling. Upon cooling, CP conditions change such that the Cp* and Me resonances quickly diminish until reaching −60 °C when both signals can no longer be detected. With further cooling, the Me and Cp* peaks slowly reappear with broader linewidths. The width at half-height ($\Delta\nu_{1/2}$) of the Cp* and Me isotropic peaks change from 81 and 84 Hz at ambient temperature to 540 and 176 Hz at −100 °C, respectively. The dramatic change in CP conditions and broad peak widths at lower temperatures suggest a change in the rate of the Cp* fivefold reorientation. Furthermore, the significantly increased TRAPDOR effect at low temperatures indicates an increase in ^{13}C-^{9}Be dipolar coupling, supporting the notion of decelerating Cp*

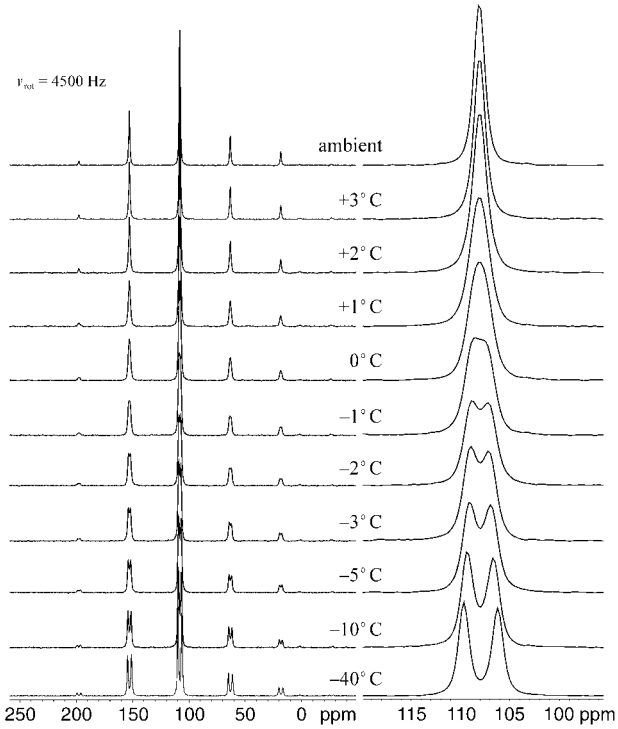

Figure 6. ^{13}C VT CP/MAS spectra employed for calculation of the activation energy (E_a = 36.9 kJ mol^{-1}) for Cp ring 'inversion' in **1**. Expansion of the isotropic resonances for each of the spectra are shown on the right.

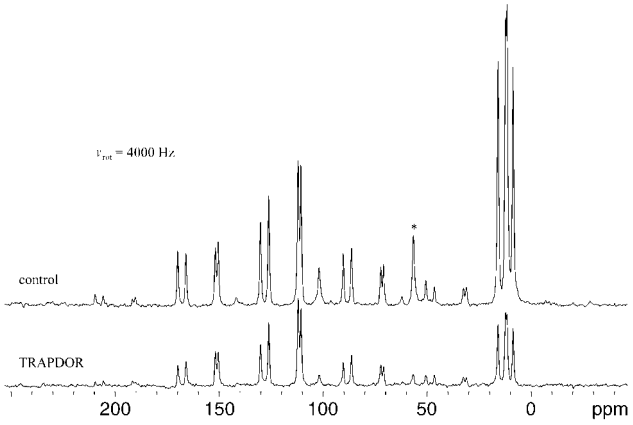

Figure 7. ^{13}C/^{9}Be/^{1}H CP/TRAPDOR spectra of **3**; asterisk (*) marks the η^1:*i*-C_5Me_4H carbon resonance.

ring motion (at −100 °C, the methyl and aromatic Cp* signals retain about 8 % and 46 % of their integrated intensity compared to the control experiment). Variable contact time experiments (ct = 0.1–25.0 ms) were also performed (not shown) to examine the reason for loss in CP efficiency between −20 °C and −80 °C, however, spectra displayed no difference to those shown in Figure 8. The peak at δ_{iso} = 2 ppm, which becomes more prevalent at lower temperatures, most likely arises from an impurity in the sample.

Theoretical calculations: Theoretical ^{9}Be CS tensors (Table 4), obtained from calculations with standard methods

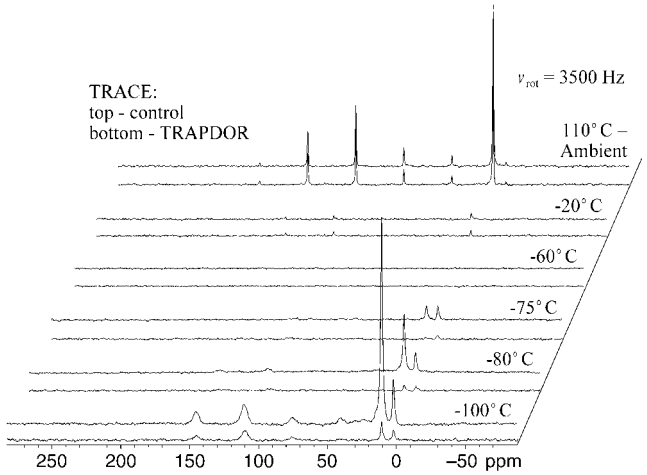

Figure 8. ^{13}C/^{9}Be/^{1}H VT CP/TRAPDOR spectra of **2**. Variable contact time experiments display no difference compared to the spectra shown.

and basis sets show remarkable agreement with experimental data. In particular, both the RHF and B3LYP methods perform exceptionally well in calculating δ_{iso} and Ω for all three compounds. The values of κ show the largest discrepancy with measured values, however, even those deviations are minute.

Calculated values of C_Q and η_Q (Table 5) also show very good agreement with experimental values. Notably, B3LYP/6–31G** calculations yield the best agreement with measured values for **1** and **3**, although all other calculations also perform well. Relatively large deviations are seen for the calculated C_Q and η_Q values of **2**. These discrepancies are attributed to rapid reorientation of the Cp* rings in **2**, which motionally averages the V_{33} component of the ^{9}Be EFG tensor and is unaccounted for in calculations (vide infra).

Not surprisingly, theoretical ^{9}Be EFG and CS tensor orientations do not vary due to the methods and basis set used. In all three cases the beryllium CS tensor has near-axial symmetry (**1**: κ = 0.83(4); **2**: κ = 0.86(7); **3**: κ = 0.85(8)) indicating that the σ_{11} and σ_{22} components are similar in magnitude while σ_{33} is distinct. Therefore, σ_{11} and σ_{22} should point towards similar electronic environments, with σ_{33} assuming an orientation along a unique symmetry element or molecular axis. Indeed, σ_{33} points in the general direction of the Cp′ ring centroid for all three compounds, while the σ_{11} and σ_{22} components lie on a plane parallel to the η^5-Cp′ moieties (Figure 9). The ^{9}Be EFG tensors of **1** and **3** are also indicative of high cylindrical ground state electronic symmetry (**1**: η_Q = 0.25(5); **3**: η_Q = 0.13(7)), consequently, theoretical EFG tensors have the V_{33} component aligned toward the Cp′ centroid also. However, the NMR interaction tensors for both **1** and **3** are not coincident. In **3**, V_{11} and σ_{22} are coincident, and $\measuredangle V_{33}$-Be-σ_{33} and $\measuredangle V_{22}$-Be-σ_{11} are equal to 4.3° (Figure 9c); the corresponding Euler angles describing the relative orientation of the two theoretical tensors are α = 90.0°, β = 4.3°, and γ = 0.0°, in very good agreement with experimentally measured values (α = 90°, β = 4(2)°, γ = 0°). For **1**, V_{33} and σ_{33} are offset by a V_{33}-Be-σ_{33} angle of 7°, while $\measuredangle V_{22}$-Be-σ_{11} and $\measuredangle V_{11}$-Be-σ_{22} are both approximately 28°

Table 4. Experimental and theoretical beryllium chemical shift tensors.

Source	δ_{11} [ppm][a]	δ_{22} [ppm]	δ_{33} [ppm]	δ_{iso} [ppm]	Ω [ppm]	κ
			[Cp_2Be]			
experimental	2.5	−3.0	−62.5	−21(1)	65(2)	0.83(4)
RHF/6–31G**	4.7	2.8	−62.3	−18.3	67.0	0.94
RHF/6–311G**	4.2	2.5	−64.0	−19.1	68.1	0.95
RHF/6–311+G**	4.7	2.7	−63.9	−18.8	68.6	0.94
B3LYP/6–31G**	3.8	1.4	−62.0	−18.9	65.8	0.93
B3LYP/6–311G**	3.3	1.5	−64.5	−19.9	67.8	0.95
B3LYP/6–311+G**	3.3	1.4	−64.5	−19.9	67.8	0.95
			[Cp^*_2Be]			
experimental	−4.8	−8.6	−59.8	−24.4(7)	55(5)	0.86(7)
RHF/6–31G**	−8.9	−9.3	−65.0	−27.7	56.1	0.98
RHF/6–311G**	−13.4	−13.7	−68.3	−31.8	54.9	0.99
RHF/6–311+G**	−13.1	−13.5	−68.2	−31.6	55.1	0.99
B3LYP/6–31G**	2.4	1.6	−51.2	−15.8	53.6	0.97
B3LYP/6–311G**	−2.1	−2.7	−54.2	−19.7	52.0	0.98
B3LYP/6–311+G**	1.2	−1.2	−53.0	−17.7	54.1	0.91
			[$(C_5Me_4H)_2Be$]			
experimental	−0.5	−4.5	−54.5	−19.8(5)	54(4)	0.85(8)
RHF/6–31G**	1.8	−2.8	−54.0	−18.4	55.8	0.83
RHF/6–311G**	0.9	−3.0	−55.8	−19.3	56.6	0.86
RHF/6–311+G**	1.2	−2.8	−55.5	−19.0	56.7	0.86
B3LYP/6–31G**	1.5	−3.2	−53.0	−18.2	54.5	0.83
B3LYP/6–311G**	0.8	−3.3	−55.5	−19.3	56.3	0.86
B3LYP/6–311+G**	1.7	−3.2	−55.2	−18.9	56.8	0.83

[a] Absolute chemical shielding values were converted to chemical shifts with the formula $\sigma_{ref}-\sigma_{sample}$, where σ_{ref} is the absolute chemical shielding of $[Be(H_2O)_4]^{2+}$ (see Experimental Section).

Table 5. Experimental and theoretical ^{9}Be EFG parameters.

Source	V_{11} [a.u.][a]	V_{22} [a.u.]	V_{33} [a.u.]	$\lvert C_Q\rvert$ [MHz]	η_Q
		[Cp_2Be]			
experimental	–	–	–	0.41(2)	0.25(5)
RHF/6–31G**	−0.0129	−0.0182	0.0311	0.39	0.17
RHF/6–311G**	−0.0092	−0.0148	0.0240	0.30	0.23
RHF/6–311+G**	−0.0093	−0.0148	0.0241	0.30	0.23
B3LYP/6–31G**	−0.0125	−0.0205	0.0330	0.41	0.24
B3LYP/6–311G**	−0.0103	−0.0193	0.0296	0.37	0.30
B3LYP/6–311+G**	−0.0104	−0.0192	0.0296	0.37	0.30
		[Cp^*_2Be]			
experimental	–	–	–	0.23(2)	0.55(5)
RHF/6–31G**	0.0102	0.0263	−0.0364	0.45	0.44
RHF/6–311G**	0.0155	0.0308	−0.0464	0.58	0.33
RHF/6–311+G**	0.0155	0.0309	−0.0464	0.58	0.33
B3LYP/6–31G**	0.0103	0.0245	−0.0349	0.43	0.41
B3LYP/6–311G**	0.0164	0.0307	−0.0470	0.59	0.30
B3LYP/6–311+G**	0.0163	0.0306	−0.0469	0.58	0.30
		[$(C_5Me_4H)_2Be$]			
experimental	–	–	–	0.61(5)	0.13(7)
RHF/6–31G**	−0.0270	−0.0315	0.0585	0.73	0.08
RHF/6–311G**	−0.0270	−0.0290	0.0559	0.70	0.04
RHF/6–311+G**	−0.0268	−0.0296	0.0563	0.70	0.05
B3LYP/6–31G**	−0.0235	−0.0306	0.0541	0.67	0.13
B3LYP/6–311G**	−0.0269	−0.0301	0.0571	0.71	0.06
B3LYP/6–311+G**	−0.0267	−0.0308	0.0574	0.72	0.07

[a] V_{ii} are the principal components of the EFG tensor, where $|V_{33}|\geq|V_{22}|\geq|V_{11}|$.

apart (Figure 9a); the theoretical Euler angles obtained are $\alpha=3.8°$, $\beta=7.0°$ and $\gamma=57.9°$. These stand in contrast to the relative orientation measured experimentally; however, one must bear in mind that simulation parameters extracted from NMR spectra are from a motionally averaged structure wherein different intramolecular dynamic processes obviously affect the NMR interactions observed, whereas theoretical results are derived from purely stationary structures. Furthermore, since both the experimental ^{9}Be EFG and CS tensors are axial, and the magnitudes of both the span and quadrupolar interaction result in rather small anisotropic frequency spreads, the relative orientation of the lesser components (V_{ii} and δ_{ii}; $i=1, 2$) with respect to each other is of minor influence and observations show misalignment only between V_{33} and δ_{33} ($\alpha=0°$, $\beta=38(5)°$, $\gamma=0°$).

The theoretical ^{9}Be EFG tensor of **2** takes on a very distinct orientation compared to those of **1** and **3** as shown in Figure 9b. In particular, the plane in which V_{22}, V_{33} and the Be atom lie makes an angle of 46° with σ_{22}, while V_{11} approximately bisects the angle between σ_{11} and σ_{22}. The corresponding Euler angles relating the orientation of the EFG and CS tensors are $\alpha=89.3°$, $\beta=29.8°$ and $\gamma=46.9°$. Simulations of the static ^{9}Be NMR spectrum of **2** using the theoretical Euler angles provide very good agreement; in fact, the experimental values ($\alpha=90°$, $\beta=28°$, $\gamma=44°$) were arrived at by only minor refinement of the calculated values. As in the case of $[Cp_2Mg]$,[43] offset of V_{33} from the Cp* centroid suggests slight distortions in the spherical/cylindrical ground state symmetry of the molecule. Indeed, the crystal structure of **2**[37] reveals that the $[Cp^*_2Be]$ unit has C_i rather than D_{5d} symmetry. For **2**, the V_{33} component tilts towards the two Cp* carbon atoms which lie farthest from the Be (Be–C distances range from 1.969 to 2.114 Å). Because of the misalignment of V_{33} from the ring centroid, fivefold reorientation of the Cp* rings reduces $C_Q(^9Be)$ so that only an average value is detected, in contrast to the values obtained from calculations.

To further explore the effects upon the ^{9}Be NMR interaction tensors from movement of the Be atom between the

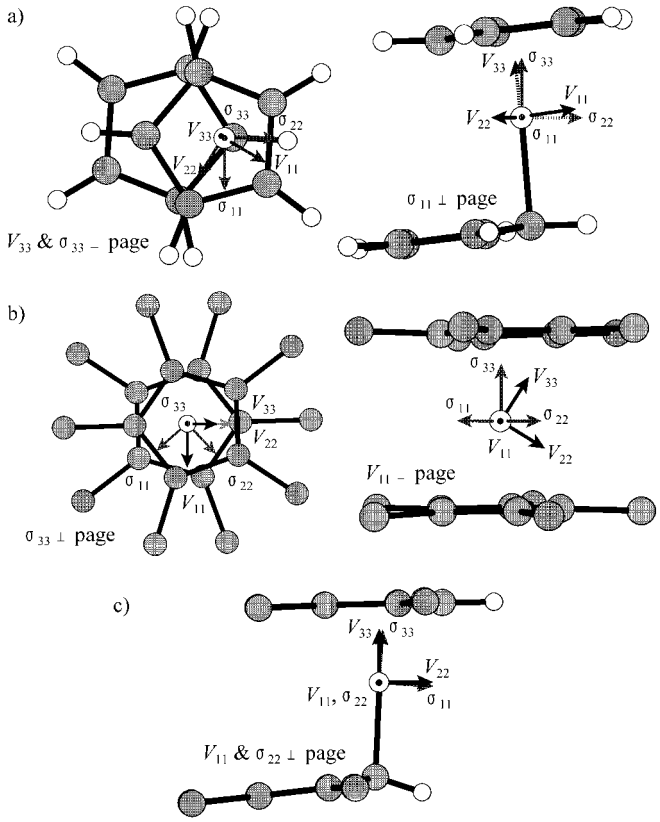

Figure 9. Theoretical ^{9}Be EFG and CS tensors of a) **1** (top and side view of molecule), b) **2** (top and side view of molecule), and c) **3**. Methyl hydrogen atoms have been omitted in **2** and **3** for clarity.

two half-occupied crystallographic sites of [Cp_2Be], a series of B3LYP/6–311G** calculations were performed attempting to simulate the suspected "inversion" process or "shuttling" motion of the Be atom. For each calculation, the Be atom was positioned at a different distance (a multiple of 1/8 of the total distance between the two crystallographic Be sites) along a straight line which joins the two crystallographic Be sites in the low-temperature structure. Calculations for five different Be positions were done in total, beginning at one of the crystallographic sites and ending at the midpoint between the two crystallographic sites (hitherto referred to as the "midpoint"); the remaining points on the other side of the midpoint were assumed to be equivalent to those calculated. The calculated ^{9}Be NMR parameters at each of the points are shown in Table 6, where the Be positions are labeled by their distance from the midpoint, that is, the 0.652 Å site is the crystallographic site. According to calculations, the "inversion" process has a classical energy barrier of 11.07 kJ mol^{-1} with the lowest and highest energies found for 0.489 Å and the midpoint, respectively. The calculated barrier is comparable to values determined from MD calculations (8 kJ mol^{-1})[36] and solution ^{13}C VT NMR spectroscopy (5.2 kJ mol^{-1}).[31] Variation of the self-consistent field energy along the reaction coordinate can be fit to the function $f(r) = A + B\cos^2(r) + C\cos^4(r) + D\cos^6(r)$ within the range $r = 0.652$ to -0.652 Å, where r is the distance from the midpoint, $A = 212.1(1.7)$, $B = -645.9(6.3)$, $C = 602.0(7.8)$ and $D = -157.2(3.2)$. The expectation value for r is 0.5996 Å as opposed to the lowest energy position which lies 0.4894 Å from the midpoint. If the trends observed from calculations are representative of the solid-state "inversion" barrier, the beryllium in [Cp_2Be] would be undergoing hindered passage between the two half-occupied sites, spending the majority of the time approximately 0.052 Å from each of the crystallographic sites.

Table 6. Theoretical (B3LYP/6–311G**) ^{9}Be EFG and CS parameters at different beryllium stationary points along the reaction coordinates of the 'inversion' process.

Parameter	Absolute distance from center position [Å]				
	0.000	0.163	0.326	0.489	0.652
$\lvert C_Q \rvert$ [MHz]	1.58	1.48	1.21	0.83	0.49
η_Q	0.77	0.74	0.63	0.39	0.05
V_{11} [a.u.]	−0.014539	−0.015539	−0.017930	−0.020133	−0.018486
V_{22} [a.u.]	−0.112587	−0.103642	−0.079196	−0.046134	−0.020617
V_{33} [a.u.]	0.127126	0.119180	0.097126	0.066267	0.039103
δ_{iso} [ppm]	−22.99	−22.79	−22.22	−21.24	−19.62
Ω [ppm]	67.96	67.35	66.11	65.50	66.95
κ	0.976	0.976	0.974	0.961	0.924
δ_{11} [ppm]	−0.06	−0.07	0.11	1.02	3.55
δ_{22} [ppm]	−0.89	−0.89	−0.77	−0.26	0.99
δ_{33} [ppm]	−68.02	−67.42	−66.00	−64.48	−63.40

In addition, according to calculations the ^{9}Be NMR interactions are also expected to vary because of the "inversion" process (Table 6, see Figure 3 in the Supporting Information for details). In moving from one of the crystallographic sites to the other, $C_Q(^9\text{Be})$ and η_Q vary within the ranges 0.49–1.58 MHz and 0.05–0.77, respectively, being greatest at the midpoint in both cases. Similarly, in going from 0.652 Å to the midpoint, κ increases to 0.976 from 0.924, while Ω varies by merely 2.46 ppm. As discussed above, the Be atom spends most of its time at or near the crystallographic sites rather than at the midpoint, explaining why NMR parameters calculated using the atomic positions from the crystal structure display such good agreement with experimental values. Thus, the observed ^{9}Be NMR signal arises almost entirely from beryllium occupying the crystallographic sites (or nearby positions). The orientation of both the theoretical ^{9}Be EFG and CS tensors display little variation along the chosen Be atom trajectory.

Conclusion

Through a combination of solid-state ^{9}Be and ^{13}C NMR spectroscopy, X-ray diffraction and molecular orbital calculations, the relationships between anisotropic NMR interactions and molecular structure and dynamics in [Cp_2Be], [Cp^*_2Be] and [$(C_5Me_4H)_2Be$] are elucidated. Notably, parameters measured by solid-state MAS and static ^{9}Be NMR experiments are correlated with molecular structure, which confirm geometries measured by X-ray diffraction: 1) $C_Q(^9\text{Be})$ increases in magnitude as the degree of spherical symmetry about the Be nuclei decreases, 2) large beryllium chemical shift anisotropies which are comparable to the entire known beryllium chemical shift range are consistent with p–π bonding to Cp′ moieties, and 3) the isotropic ^{9}Be

chemical shift increases as the overall hapticity is decreased, that is, δ_{iso} increases in the order: $[Cp^*_2Be]$ (η^5,η^5), $[Cp'_2Be]$ (η^5,η^{1-3}), and $[(C_5Me_4H)_2Be]$ (η^5,η^1). On the other hand, variable-temperature NMR experiments allow examination of intramolecular dynamics: VT ^{9}Be NMR experiments reveal that a small portion of $[Cp_2Be]$ molecules undergo rapid isotropic motion even at ambient temperature and that $[Cp^*_2Be]$ and $[(C_5Me_4H)_2Be]$ undergo relatively small variation in their molecular geometries with changing temperature. ^{13}C VT CP/MAS NMR spectra of $[Cp_2Be]$ reveal chemical exchange, indicating that the hapticities of the Cp rings are 'inverted' through the motion of the beryllium atom between the crystallographically equivalent sites; the activation energy associated with this 'inversion' process is measured to be 36.9 kJ mol^{-1}. In the case of $[Cp^*_2Be]$, ^{13}C/^{9}Be/^{1}H VT CP/TRAPDOR spectra show dramatic changes upon cooling, which indicate a slowing down of the fivefold reorientation of the Cp* ring.

Ab initio (RHF) and hybrid density functional theory (B3LYP) calculations yield excellent agreement with experimental NMR interaction parameters. In combination with experimental data, theoretical calculations give a particularly good indication as to the equilibrium geometry found in the condensed phase of $[Cp_2Be]$, namely, that the Be atom spends most of its time located at one of the two related crystallographic sites and a relatively insignificant amount of time in transit. Theoretical calculations aid in determining the orientation of anisotropic NMR interaction tensors in the molecular frame, which further correlates NMR parameters with molecular structure. We hope to have shown that solid-state NMR spectroscopy is an excellent complimentary technique to X-ray diffraction for confirming molecular symmetry, rapid checking of sample purity, relating magnetic shielding tensors to molecular structure and enabling the observation of unique solid-state intramolecular dynamics.

Experimental Section

Compounds **1–3** were prepared using literature procedures.[3,37] ***CAUTION:*** *Extreme care must be taken in dealing with beryllium compounds because they are very toxic and can cause serious irreversible effects.*

X-ray crystallography: Crystalline samples of each of the beryllocenes were obtained by cooling saturated pentane solutions of the compounds to −30 °C. In a glove box containing a dry N_2 atmosphere, the data crystals were selected and mounted in thin-walled glass capillaries, which were subsequently flame-sealed. The sealed capillaries were affixed to brass specimen pins using epoxy. A Kryo-Flex low temperature device was used for low-temperature experiments. Note that the same crystal of $[Cp_2Be]$ was used to collect data at both 20 °C and −100 °C. The data were collected on a Bruker APEX CCD diffractometer using a graphite monochromator with $Mo_{K\alpha}$ radiation ($\lambda = 0.71069$ Å). A hemisphere of data was collected using a counting time of 30 s per frame. Details of crystal data, data collection and structure refinement are listed in Table 1. Data reduction was performed by using the SAINT software[75] and the data were corrected for Lorentz, polarization and absorption effects using the SAINT and SADABS programs. The structures were solved by direct methods using SIR97[76] and refined by full-matrix least-squares on F^2 with anisotropic displacement parameters for the non-H atoms using SHELXL-97.[77] Neutral atom scattering factors and values used to calculate the linear absorption coefficient are from the *International Tables for X-ray Crystallography* (**1992**).[78] Hydrogen atoms were placed in calculated positions and were assigned coupled isotropic temperature factors using an appropriate riding model.[79] CCDC-234475–CCDC-234478 contain the supplementary crystallographic data for this paper. These data can be obtained free of charge via www.ccdc.cam.ac.uk/conts/retrieving.html (or from the Cambridge Crystallographic Data Centre, 12, Union Road, Cambridge CB21EZ, UK; fax: (+44) 1223-336-033; or deposit@ccdc.cam.ac.uk).

Solid-state NMR spectroscopy: ^{9}Be and ^{13}C NMR spectra were acquired on a Varian Infinity Plus NMR spectrometer with an Oxford $B_0 = 9.4$ T ($\nu_0(^1H) = 400$ MHz) wide bore magnet operating at $\nu_0(^9Be) = 56.2$ MHz and $\nu_0(^{13}C) = 100.5$ MHz. Samples were finely powdered and packed under a nitrogen atmosphere into 4 mm outer diameter ZrO_2 rotors.

Central transition selective $\pi/2$ pulse widths of 0.67, 1.0, and 2.2 μs with rf fields of $\nu_1 = 62.5$, 41.7, and 56.8 kHz, spectral widths (sw) of 40, 40, and 20 kHz, and recycle delays of 2.1, 10, and 20 s were employed, respectively, for the static ^{9}Be NMR spectra of **1–3**. The ^{9}Be MAS spectrum of **3** was acquired with the same parameters as the static spectrum but with a 10 kHz spectral window. For the ^{9}Be SATRAS spectra of **1** and **2**, central transition selective $\pi/2$ pulse widths of 1.5 and 2.25 μs with rf fields of $\nu_1 = 90.9$ and 55.6 kHz and recycle delays of 4 and 15 s were employed, respectively.

The $^{13}C\{^1H\}$ CP/MAS spectra of **1** were acquired at $\nu_{rot} = 1415$ and 4500 Hz with a proton $\pi/2$ pulse of 5.5 μs, contact time (ct) of 15 ms, sw = 40 kHz and recycle delay of 10 s; for **2**: $\nu_{rot} = 1040$ and 3500 Hz, proton $\pi/2$ pulse = 2.75 μs, ct = 9 ms, sw = 50 kHz and recycle delay = 15 s, while for **3**: $\nu_{rot} = 4000$ and 15000 Hz, proton $\pi/2$ pulse = 4.5 μs, ct = 15 ms, sw = 50 kHz and recycle delay = 20 s. Variable-temperature (VT) $^{13}C/^9Be/^1H$ CP/TRAPDOR (TRAnsfer of Populations in DOuble Resonance) experiments on all three species were recorded in a similar fashion as CP/MAS spectra with additional on-resonance irradiation of beryllium nuclei over one rotor period with rf fields of about 30, 40, and 60 kHz for **1–3**.

Central transition selective pulse widths are non-selective pulse widths which have been scaled by a factor of $(I + 1/2)^{-1}$. Beryllium chemical shifts were referenced to a concentrated aqueous solution of $BeCl_2$ ($\delta_{iso} = 0.0$ ppm); carbon shifts are reported with respect to the $Si(CH_3)_4$ scale ($\delta_{iso} = 0.0$ ppm) by setting the chemical shift of the adamantane high-frequency resonance to 38.57 ppm. Variable-temperature experiments were performed within a temperature range of 110 °C to −120 °C with an accuracy of ±1 °C at the extremes.

Spectral simulations: Analytical simulations of ^{9}Be static and MAS NMR spectra were performed with the WSOLIDS software package written and developed by K. Eichele in R. E. Wasylishen's laboratory at Dalhousie University. Further refinement of quadrupolar parameters for the SATRAS NMR spectra of **1** and **2** was obtained by numerical simulations with the SIMPSON software package.[80] SIMPSON simulations were accomplished by the direct method of powder averaging using the zcw4180 crystal file provided with the package. The gamma angles parameter was set to (sw/ν_{rot}), where sw is the spectral width and ν_{rot} is the rate of spinning; in the case of **2**, sw had to be increased to 301.5 kHz to accommodate the equation for the gamma angles. The start and detect operators were set to I_{1z} and I_{1p}, respectively, while all other parameters were set equal to those employed experimentally. Simulated spectra were saved in ASCII format as free induction decay (FID) files without any mathematical manipulation and converted to files readable by the NUTS (Acorn NMR) software for further processing. Best-fit spectra were obtained by comparison of root-mean-square difference spectra, and experimental errors for the extracted NMR parameters were determined by bidirectional variation. All experimental carbon chemical shift tensors were obtained by analysis of ^{13}C NMR spectra with the method of Herzfeld and Berger.[81,82]

Conventions used for the specification of electric field gradient and chemical shift parameters differ between the WSOLIDS and SIMPSON simulation programs, and therefore, the reader is alerted to these differences. Whereas WSOLIDS uses the right-handed EFG and chemical shift tensors given by ($|V_{zz}| \geq |V_{yy}| \geq |V_{xx}|$; $C_Q = eV_{zz}Qh^{-1}$; $\eta_Q = (V_{xx} - V_{yy})/V_{zz}$) and ($\delta_{11} \geq \delta_{22} \geq \delta_{33}$; $\Omega = \delta_{11} - \delta_{33}$; $\kappa = 3(\delta_{22} - \delta_{iso})/\Omega$), respectively, the conventions employed in SIMPSON differ ($|V_{zz}| \geq |V_{xx}| \geq |V_{yy}|$; $C_Q = eV_{zz}Qh^{-1}$; $\eta_Q = (V_{yy} - V_{xx})/V_{zz}$; $|\delta_{zz} - \delta_{iso}| \geq |\delta_{xx} - \delta_{iso}| \geq |\delta_{yy} - \delta_{iso}|$; $\delta = \delta_{zz} - \delta_{iso}$; $\kappa = (\delta_{yy} - \delta_{xx})/\delta$). In cases where the chemical shift and EFG tensors do not coincide, Euler angles are implemented to describe their relative orientation. One must be cautious in selecting Euler angles

appropriate to the convention implemented within the simulation software. The WSOLIDS conventions are followed in the present work. Namely, the Euler angles α, β, and χ are employed for unitary transformations in the order $\mathbf{R}_{z''}(\chi)\mathbf{R}_{y'}(\beta)\mathbf{R}_{z}(\alpha)$,[83,84] where $\mathbf{R}_i(\theta)$ performs a counter-clockwise (positive) rotation about the positive i axis by angle θ, producing a new rotation axis i', such that a coordinate system initially coincident with the EFG principal axis system (PAS) ends up coincident with the chemical shift PAS after the transformation (i.e., an active transformation).

Theoretical calculations: Calculations of EFG and chemical shielding tensors were performed using Gaussian 98[85] on a Dell Precision 420 workstation with dual 733 MHz Pentium III processors running the Red Hat Linux 6.2 operating system. Calculations were done on isolated molecules with molecular coordinates obtained from the crystal structures resolved by X-ray diffraction.[32,37] Computations were carried out using restricted Hartree–Fock (RHF) and hybrid density functional theory (DFT) with the B3LYP functional,[86–88] and the 6–31G**, 6–311G** and 6–311+G** basis sets for all nuclei. Quadrupole coupling constants (C_Q) were converted from atomic units (a.u.) to MHz by multiplying the largest component of the EFG tensor, V_{33}, by $eQh^{-1} \times 9.71736 \times 10^{21}\ \mathrm{V\,m^{-2}}$, where Q (^{9}Be) $= 5.3 \times 10^{-30}\ \mathrm{m^2}$,[52,53] and $e = 1.602188 \times 10^{-19}$ C. Chemical shielding tensors were calculated using the GIAO method[89,90] excluding relativistic effects. Calculated beryllium shielding data was referenced by setting the theoretical isotropic chemical shielding of $[Be(H_2O)_4]^{2+}$ to $\delta_{iso} = 0.0$ ppm. Similarly, carbon CS tensors were referenced to the theoretical shielding of CO as a secondary reference by subtracting the theoretical shielding data of the compound from that of CO (calculated with the corresponding theoretical method and basis set) and then adding $\delta_{iso}(CO) = 187.1$ ppm.[91]

Acknowledgement

This research was funded by Imperial Oil and the Natural Sciences and Engineering Research Council (NSERC - Canada). R.W.S. is also grateful to the Canadian Foundation for Innovation (CFI), the Ontario Innovation Trust (OIT), and the University of Windsor for providing funding for equipment in the Solid-State Laboratories at the University of Windsor, including the Solid-State NMR Facility and X-ray diffractometers. I.H. thanks the Centre for Catalysis and Materials Research (CCMR) at the University of Windsor for a graduate research scholarship.

[1] E. O. Fischer, H. P. Hofmann, *Chem. Ber.* **1959**, *92*, 482.
[2] H. P. Fritz, R. Schneider, *Chem. Ber.* **1960**, *93*, 1171.
[3] H. P. Fritz, *Chem. Ber.* **1959**, *92*, 780.
[4] A. Almenningen, O. Bastiansen, A. Haaland, *J. Chem. Phys.* **1964**, *40*, 3434.
[5] M. Sundbom, *Acta Chem. Scand.* **1966**, *20*, 1608.
[6] G. B. McVicker, G. L. Morgan, *Spectrochimica Acta Part A* **1970**, *26*, 23.
[7] H. P. Fritz, D. Sellmann, *J. Organomet. Chem.* **1966**, *5*, 501.
[8] O. Y. Lopatko, N. M. Klimenko, M. E. Dyatkina, *J. Struct. Chem.* **1972**, *13*, 1044.
[9] S. P. Ionov, G. V. Ionova, *Izvestiia Akademii nauk SSR, Seriia Khimiia* **1970**, 2836.
[10] C.-H. Wong, T.-Y. Lee, K.-J. Chao, S. Lee, *Acta Crystallogr. Sect. B* **1972**, *28*, 1662.
[11] D. A. Drew, A. Haaland, *Acta Crystallogr. Sect. B* **1972**, *28*, 3671.
[12] C.-H. Wong, K. J. Chao, C. Chih, T. Y. Lee, *J. Chin. Chem. Soc.* **1969**, *16*, 15.
[13] C. Wong, T. Y. Lee, T. J. Lee, T. W. Chang, C. S. Liu, *Inorg. Nucl. Chem. Lett.* **1973**, *9*, 667.
[14] G. L. Morgan, G. B. McVicker, *J. Am. Chem. Soc.* **1968**, *90*, 2789.
[15] C.-H. Wong, S.-M. Wang, *Inorg. Nucl. Chem. Lett.* **1975**, *11*, 677.
[16] J. B. Collins, P. V. R. Schleyer, *Inorg. Chem.* **1977**, *16*, 152.
[17] D. S. Marynick, *J. Am. Chem. Soc.* **1977**, *99*, 1436.
[18] C.-S. Liu, *J. Chin. Chem. Soc.* **1977**, *24*, 79.
[19] J. Demuynck, M. M. Rohmer, *Chem. Phys. Lett.* **1978**, *54*, 567.
[20] M. J. S. Dewar, H. S. Rzepa, *J. Am. Chem. Soc.* **1978**, *100*, 777.
[21] N.-S. Chiu, L. Schaefer, *J. Am. Chem. Soc.* **1978**, *100*, 2604.
[22] E. D. Jemmis, S. Alexandratos, P. v. R. Schleyer, A. Streitwieser, Jr., H. F. Schaefer, III, *J. Am. Chem. Soc.* **1978**, *100*, 5695.
[23] O. P. Charkin, A. Veillard, J. Demuynck, M. M. Rohmer, *Koord. Khim.* **1979**, *5*, 501.
[24] R. Gleiter, M. C. Boehm, A. Haaland, R. Johansen, J. Lusztyk, *J. Organomet. Chem.* **1979**, *170*, 285.
[25] C. Glidewell, *J. Organomet. Chem.* **1981**, *217*, 273.
[26] L. A. Gribov, M. M. Raikhshtat, V. V. Zhogina, *Koord. Khim.* **1988**, *14*, 1368.
[27] J. Lusztyk, K. B. Starowieyski, *J. Organomet. Chem.* **1979**, *170*, 293.
[28] S. J. Pratten, M. K. Cooper, M. J. Aroney, *Polyhedron* **1984**, *3*, 1347.
[29] S. J. Pratten, M. K. Cooper, M. J. Aroney, S. W. Filipczuk, *J. Chem. Soc. Dalton Trans.* **1985**, 1761.
[30] K. W. Nugent, J. K. Beattie, *J. Chem. Soc. Chem. Commun.* **1986**, 186.
[31] K. W. Nugent, J. K. Beattie, L. D. Field, *J. Phys. Chem.* **1989**, *93*, 5371.
[32] K. W. Nugent, J. K. Beattie, T. W. Hambley, M. R. Snow, *Aust. J. Chem.* **1984**, *37*, 1601.
[33] K. W. Nugent, J. K. Beattie, *Inorg. Chem.* **1988**, *27*, 4269.
[34] R. Car, M. Parrinello, *Phys. Rev. Lett.* **1985**, *55*, 2471.
[35] P. Margl, K. Schwarz, P. E. Bloechl, *J. Am. Chem. Soc.* **1994**, *116*, 11177.
[36] P. Margl, K. Schwarz, P. E. Blochl, *J. Chem. Phys.* **1995**, *103*, 683.
[37] M. D. Conejo, R. Fernandez, E. Gutierrez-Puebla, A. Monge, C. Ruiz, E. Carmona, *Angew. Chem.* **2000**, *112*, 2025; *Angew. Chem. Int. Ed.* **2000**, *39*, 1949.
[38] M. D. Conejo, R. Fernandez, D. del Rio, E. Carmona, A. Monge, C. Ruiz, *Chem. Commun.* **2002**, 2916.
[39] M. D. Conejo, R. Fernandez, D. del Rio, E. Carmona, A. Monge, C. Ruiz, A. M. Marquez, J. F. Sanz, *Chem. Eur. J.* **2003**, *9*, 4452.
[40] M. D. Conejo, R. Fernandez, E. Carmona, E. Gutierrez-Puebla, A. Monge, *Organometallics* **2001**, *20*, 2434.
[41] M. D. Conejo, R. Fernandez, E. Carmona, R. A. Andersen, E. Gutierrez-Puebla, M. A. Monge, *Chem. Eur. J.* **2003**, *9*, 4462.
[42] D. L. Bryce, R. E. Wasylishen, *J. Phys. Chem. A* **1999**, *103*, 7364.
[43] I. Hung, R. W. Schurko, *Solid State Nucl. Magn. Reson.* **2003**, *24*, 78.
[44] R. W. Schurko, I. Hung, C. L. B. Macdonald, A. H. Cowley, *J. Am. Chem. Soc.* **2002**, *124*, 13204.
[45] R. W. Schurko, I. Hung, S. Schauff, C. L. B. Macdonald, A. H. Cowley, *J. Phys. Chem. A* **2002**, *106*, 10096.
[46] D. Johnels, B. A. , U. Edlund, *Magn. Reson. Chem.* **1998**, *36*, S151.
[47] T. Pietrass, P. K. Burkert, *Inorg. Chim. Acta* **1993**, *207*, 253.
[48] C. Janiak, H. Schumann, C. Stader, B. Wrackmeyer, J. J. Zuckerman, *Chem. Ber.* **1988**, *121*, 1745.
[49] B. Wrackmeyer, E. Kupce, G. Kehr, A. Sebald, *Magn. Reson. Chem.* **1992**, *30*, 964.
[50] H. W. Spiess, H. Haas, H. Hartmann, *J. Chem. Phys.* **1969**, *50*, 3057.
[51] J. M. Keates, G. A. Lawless, *Organometallics* **1997**, *16*, 2842.
[52] D. Sundholm, J. Olsen, *Chem. Phys. Lett.* **1991**, *177*, 91.
[53] P. Pyykko, *Z. Naturforsch. Teil. A* **1992**, *47*, 189.
[54] L. C. Brown, D. Williams, *J. Chem. Phys.* **1956**, *24*, 751.
[55] J. F. Hon, *Phys. Rev.* **1961**, *124*, 1368.
[56] G. J. Troup, J. Walter, *J. Nucl. Mater.* **1964**, *14*, 272.
[57] H. L. Reaves, T. E. Gilmer, Jr., *J. Chem. Phys.* **1965**, *42*, 4138.
[58] R. Blinc, J. Slak, J. Stepisnik, *J. Chem. Phys.* **1971**, *55*, 4848.
[59] W. J. Dell, R. V. Mulkern, P. J. Bray, M. J. Weber, S. A. Brawer, *Phys. Rev. B* **1985**, *31*, 2624.
[60] E. T. Ahrens, P. C. Hammel, R. H. Heffner, A. P. Reyes, J. L. Smith, W. G. Clark, *Phys. Rev. B* **1993**, *48*, 6691.
[61] T. H. Yeom, A. R. Lim, S. H. Choh, K. S. Hong, Y. M. Yu, *J. Phys. Condens. Matter* **1995**, *7*, 6117.
[62] J. Skibsted, P. Norby, H. Bildsoe, H. J. Jakobsen, *Solid State Nucl. Magn. Reson.* **1995**, *5*, 239.
[63] V. D. Kodibagkar, P. A. Fedders, C. D. Browning, R. C. Bowman, Jr., N. L. Adolphi, M. S. Conradi, *Phys. Rev. B* **2003**, *67*, Art. no. 045107.
[64] D. A. Drew, G. L. Morgan, *Inorg. Chem.* **1977**, *16*, 1704.
[65] M. Kanakubo, H. Ikeuchi, G. P. Sato, *Faraday Trans.* **1998**, *94*, 3237.
[66] D. A. Saulys, D. R. Powell, *Organometallics* **2003**, *22*, 407.
[67] R. A. Kovar, G. L. Morgan, *J. Am. Chem. Soc.* **1970**, *92*, 5067.

[68] D. F. Gaines, K. M. Coleson, D. F. Hillenbrand, *J. Magn. Reson.* **1981**, *44*, 84.
[69] A. Almenningen, A. Haaland, J. Lusztyk, *J. Organomet. Chem.* **1979**, *170*, 271.
[70] T. P. Das, E. L. Hahn, *Nuclear Quadrupole Resonance Spectroscopy*, Academic Press, New York, **1958**.
[71] E. A. C. Lucken, *Nuclear Quadrupole Coupling Constants*, Academic Press, New York, **1969**.
[72] D. E. Wemmer, D. J. Ruben, A. Pines, *J. Am. Chem. Soc.* **1981**, *103*, 28.
[73] D. E. Wemmer, A. Pines, *J. Am. Chem. Soc.* **1981**, *103*, 34.
[74] C. P. Grey, A. J. Vega, *J. Am. Chem. Soc.* **1995**, *117*, 8232.
[75] Bruker AXS, Inc., Madison, WI, **2001**.
[76] A. Altomare, M. C. Burla, M. Camalli, B. Carrozzini, G. L. Cascarano, C. Giacovazzo, A. Guagliardi, A. G. G. Moliterni, G. Polidori, R. Rizzi, *J. Appl. Crystallogr.* **1999**, *32*, 115.
[77] G. M. Sheldrick, Program for the Refinement of Crystal Structures, University of Gottingen, Germany, **1997**.
[78] *International Tables for X-ray Crystallography*, *Vol. C* (Ed.: A. J. C. Wilson), Kluwer Academic Press, Boston, **1992**, Tables 4.2.6.8 and 6.1.1.4.
[79] G. M. Sheldrick, Version 6.10 ed., Bruker AXS, Inc., Madison, WI, **1994**.
[80] M. Bak, J. T. Rasmussen, N. C. Nielsen, *J. Magn. Reson.* **2000**, *147*, 296.
[81] M. M. Maricq, J. S. Waugh, *J. Chem. Phys.* **1979**, *70*, 3300.
[82] J. Herzfeld, A. E. Berger, *J. Chem. Phys.* **1980**, *73*, 6021.
[83] M. Mehring, *Principles of High Resolution NMR in Solids*, Springer, New York, **1983**.
[84] R. N. Zare, *Angular Momentum: Understanding Spatial Aspects in Chemistry and Physics*, Wiley, Toronto, **1988**.
[85] Gaussian 98, Revision A.9, M. J. Frisch, G. W. Trucks, H. B. Schlegel, G. E. Scuseria, M. A. Robb, J. R. Cheeseman, V. G. Zakrzewski, J. Montgomery, J. A., R. E. Stratmann, J. C. Burant, S. Dapprich, J. M. Millam, A. D. Daniels, K. N. Kudin, M. C. Strain, O. Farkas, J. Tomasi, V. Barone, M. Cossi, R. Cammi, B. Mennucci, C. Pomelli, C. Adamo, S. Clifford, J. Ochterski, G. A. Petersson, P. Y. Ayala, Q. Cui, K. Morokuma, D. K. Malick, A. D. Rabuck, K. Raghavachari, J. B. Foresman, J. Cioslowski, J. V. Ortiz, A. G. Baboul, B. B. Stefanov, G. Liu, A. Liashenko, P. Piskorz, I. Komaromi, R. Gomperts, R. L. Martin, D. J. Fox, T. Keith, M. A. Al-Laham, C. Y. Peng, A. Nanayakkara, M. Challacombe, P. M. W. Gill, B. Johnson, W. Chen, M. W. Wong, J. L. Andres, C. Gonzalez, M. Head-Gordon, E. S. Replogle, J. A. Pople, Gaussian, Pittsburgh, PA, **1998**.
[86] A. D. Becke, *Phys. Rev. A* **1988**, *38*, 3098.
[87] C. Lee, W. Yang, R. G. Parr, *Phys. Rev. B* **1988**, *37*, 785.
[88] A. D. Becke, *J. Chem. Phys.* **1993**, *98*, 5648.
[89] R. Ditchfield, *Molecul. Phys.* **1974**, *27*, 789.
[90] K. Wolinski, J. F. Hinton, P. Pulay, *J. Am. Chem. Soc.* **1990**, *112*, 8251.
[91] A. K. Jameson, C. J. Jameson, *Chem. Phys. Lett.* **1987**, *134*, 461.

Received: April 26, 2004
Published online: October 14, 2004

